Journal of
Composites Science

MDPI

Article

Monometallic and Bimetallic Ni–Cu Catalysts Supported on Gd-Doped CeO_2 for Hydrogen-Rich Syngas Production via Methane Partial Oxidation

Pannipa Nachai

Department of Chemistry, Faculty of Science and Technology, Thammasat University, Pathumthani 12120, Thailand; pannipa@tu.ac.th

Abstract

Partial oxidation of methane is a highly attractive route for hydrogen-rich syngas production, provided that high H_2 yields and H_2/CO ratios above 3 can be achieved. Herein, we demonstrate that precise compositional tuning of Ni–Cu bimetallic catalysts supported on Gd-doped CeO_2 enables direct control over defect chemistry and reaction pathways in partial oxidation of methane. A systematic investigation of Ni/Cu ratios was conducted to elucidate composition–structure–activity relationships using X-ray diffraction, Raman spectroscopy, temperature-programmed reduction/oxidation/desorption, and thermogravimetric analysis. While monometallic 5%Ni/GDC and promoted 1%Re4%Ni/GDC exhibited high methane conversion, they failed to deliver optimal hydrogen selectivity. In contrast, introducing Cu within a narrow compositional window fundamentally altered the reaction mechanism. The 2.5%Ni2.5%Cu/GDC catalyst showed limited oxygen vacancy formation and pronounced carbon deposition, leading to inferior catalytic performance. Remarkably, the 3.5%Ni1.5%Cu/GDC catalyst maximized both oxygen vacancy density and surface basicity, thereby selectively activating CO_2- and H_2O-assisted oxidation routes and enforcing the exclusive dominance of indirect POM pathways. This defect-mediated pathway control effectively decoupled methane activation from hydrogen-consuming side reactions while simultaneously promoting hydrogen-forming, CO-consuming reactions, most notably the water–gas shift reaction. As a result, the optimized 3.5%Ni1.5%Cu/GDC catalyst achieved an H_2 yield of 84% with an H_2/CO ratio of 3.11 and maintained stable operation for 40 h on stream at 600 °C. These findings establish Ni–Cu compositional tuning as a powerful strategy for defect engineering and reaction pathway regulation, providing new design principles for efficient and durable partial oxidation of methane catalysts targeting hydrogen-rich syngas production.

Keywords: methane partial oxidation; hydrogen-rich syngas; Ni–Cu bimetallic catalysts; Gd-doped CeO_2; oxygen vacancies

Check for updates

Academic Editor: Francesco Tornabene

Received: 25 December 2025
Revised: 17 January 2026
Accepted: 22 January 2026
Published: 28 January 2026

Copyright: © 2026 by the author. Licensee MDPI, Basel, Switzerland. This article is an open access article distributed under the terms and conditions of the Creative Commons Attribution (CC BY) license.

1. Introduction

Methane possesses a substantially stronger heat-trapping capability than carbon dioxide, resulting in a significantly higher global warming potential [1]. Consequently, the development of efficient catalysts for rapid methane abatement has become a critical challenge for climate change mitigation. Current research efforts primarily focus on catalytic pathways that convert methane into less harmful products, such as carbon dioxide and water via oxidation, or into value-added products, including hydrogen and solid carbon through catalytic decomposition. The conversion of methane to synthesis gas can be

achieved through three principal routes: partial oxidation of methane (POM), dry reforming of methane (DRM), and steam reforming of methane (SRM) [2–4]. Among these processes, SRM is highly endothermic, leading to substantial energy consumption and increased operational costs [5]. In contrast, POM has emerged as a promising and cost-effective alternative due to its high energy efficiency and its ability to produce an optimal H_2/CO ratio suitable for downstream chemical synthesis [6].

The design of catalysts for the controlled oxidation of methane to generate hydrogen-rich synthesis gas with an H_2/CO ratio exceeding 3 has attracted increasing attention, as it enables the efficient transformation of a potent greenhouse gas into a valuable feedstock for chemical synthesis. This process, commonly referred to as the partial oxidation of methane (POM), relies on the catalytic activation of methane in the presence of oxygen [7]. A high H_2/CO ratio is particularly desirable for clean energy applications, as it enhances hydrogen production, a key energy carrier in low-carbon energy systems. From a stoichiometric perspective, the direct POM reaction ($CH_4 + ½O_2 \longrightarrow 2H_2 + CO$) yields an H_2/CO ratio of 2. However, in practical catalytic systems, especially over Ni-based catalysts, H_2/CO ratios significantly higher than 2 are frequently observed. This deviation from stoichiometric predictions indicates that POM does not proceed exclusively through a direct oxidation pathway but instead involves indirect reaction routes. In the indirect POM mechanism, methane initially undergoes complete oxidation to CO_2 and H_2O. These oxidation products subsequently participate in secondary reforming reactions with additional methane, namely dry reforming ($CH_4 + CO_2$) and steam reforming ($CH_4 + H_2O$), leading to the formation of synthesis gas composed of CO and H_2. Furthermore, at relatively low reaction temperatures, the water–gas shift (WGS) reaction becomes increasingly important in enhancing hydrogen selectivity. Owing to its exothermic nature, the WGS reaction ($CO + H_2O \longrightarrow H_2 + CO_2$) is thermodynamically favored at lower temperatures, shifting the equilibrium toward increased hydrogen and carbon dioxide formation [8]. Achieving high catalytic activity under these conditions therefore requires the development of highly active and well-designed catalysts capable of efficiently driving these coupled reaction pathways.

Partial oxidation of methane is generally carried out in the presence of heterogeneous catalysts [5,9]. Noble metal-based catalysts, including Pt, Pd, Rh, and Ru, exhibit excellent catalytic activity for POM; however, their high cost and limited natural abundance severely restrict their large-scale industrial application [5,10]. As a result, supported Ni-based catalysts have been widely adopted in industrial processes due to their favorable catalytic performance combined with significantly lower cost. Despite these advantages, Ni catalysts are prone to deactivation caused by carbon deposition and particle sintering under POM operating conditions. To address these challenges, various strategies have been employed to enhance the activity and durability of Ni-based catalysts, including modification of the catalyst support, incorporation of secondary metals to form bimetallic systems, and the use of suitable promoters [11]. Among the available supports, ceria and doped ceria have attracted considerable attention because of their high oxygen storage capacity and excellent redox properties, which facilitate oxygen transfer and suppress coke formation in oxidation and reforming reactions [12,13]. Notably, gadolinium-doped ceria (GDC) has been reported to exhibit significantly lower carbon deposition compared to undoped ceria supports. This improved coke resistance is primarily attributed to the enhanced oxide ion conductivity induced by Gd doping, which promotes lattice oxygen mobility and facilitates the continuous removal of surface carbon species during reaction [14]. In general, the water–gas shift (WGS) reaction is widely employed to adjust the composition of product gas streams for downstream applications by increasing the hydrogen content [14,15]. In our previous studies, the WGS reaction was investigated as an effective route to enhance the H_2/CO ratio using Cu-based catalysts supported on CeO_2 and gadolinium-doped

ceria (GDC). The results demonstrated that the 5%Cu/GDC catalyst exhibited the highest catalytic performance, achieving approximately 80% CO conversion at 400 °C. Furthermore, the introduction of a Re promoter was found to significantly enhance the catalytic activity of Cu-based catalysts, highlighting the beneficial role of promoter addition in improving WGS performance [14].

The scope of this work is to establish design principles for high-performance Ni-based bimetallic catalysts for hydrogen-rich syngas production via the partial oxidation of methane. Rather than optimizing reaction conditions or screening catalysts empirically, this study focuses on engineering metal–support and metal–metal interactions through the use of gadolinium-doped ceria (GDC) as an advanced support. The redox flexibility and defect-rich structure of GDC are intentionally exploited to stabilize Ni active sites and to modulate oxygen mobility and reaction pathways under POM conditions.

A key objective of this work is to elucidate how the controlled incorporation of secondary metals (Cu and Re) alters the electronic and structural environment of Ni, leading to enhanced hydrogen selectivity, suppression of undesired parallel reactions, and improved resistance to carbon deposition. The novelty of this study lies in demonstrating that bimetallic synergy coupled with GDC-induced defect chemistry enables simultaneous achievement of high methane conversion and elevated H_2/CO ratios.

2. Experimental

2.1. Catalyst Preparation

All catalysts were synthesized by the incipient wetness impregnation method using gadolinium-doped ceria containing 10 mol% Gd (GDC; Daiichi Kigenso Kagaku Kogyo, Osaka, Japan) as the support. Prior to impregnation, the as-received GDC powder was mechanically ground using an agate mortar and pestle to break up agglomerates and then sieved using standard stainless-steel sieves to obtain particles in the size range of 0.30–0.60 mm. Nickel (II) nitrate hexahydrate ($Ni(NO_3)_2 \cdot 6H_2O$, Merck KGaA, Darmstadt, Germany), copper (II) nitrate trihydrate ($Cu(NO_3)_2 \cdot 3H_2O$, Sigma-Aldrich, St. Louis, MO, USA) and ammonium perrhenate (NH_4ReO_4, Sigma-Aldrich) were used as metal precursors. The total metal loading was fixed at 5 wt% for all catalysts. The prepared catalyst compositions included 5%Ni, 5%Cu, 1%Re–4%Ni, 2.5%Cu–2.5%Ni and 1.5%Cu–3.5%Ni (wt%). For impregnation, the required amount of metal precursor was dissolved in deionized water to prepare an aqueous solution with a metal ion concentration in the range of 0.8–1.2 mol L^{-1}, depending on the target composition. The total solution volume was carefully adjusted to match the measured pore volume of the GDC support. The precursor solution was then added dropwise to the GDC support under continuous stirring to ensure homogeneous distribution of metal species. After impregnation, the obtained material was aged at room temperature for 4 h to promote metal–support interaction, followed by drying at 110 °C for 12 h to remove residual moisture. The dried samples were subsequently calcined in static air at 650 °C for 8 h (heating rate: 5 °C min^{-1}), resulting in the formation of well-dispersed metal oxide species anchored on the GDC support.

2.2. Catalyst Characterization

2.2.1. Structural and Morphological Characterization

The crystalline phases of the fresh catalysts were identified by powder X-ray diffraction (XRD) using a PANalytical X'Pert Pro diffractometer (Malvern Panalytical, Almelo, The Netherlands) with Ni-filtered Cu K_α radiation (λ = 0.15418 nm). The measurements were conducted at 40 kV and 40 mA, covering a 2θ range of 20–80° with a step size of 0.02° and a counting time of 0.5 s per step. The average crystallite size of CeO_2 was

estimated from the line broadening of the most intense (111) diffraction peak using the Scherrer equation.

The surface morphology and microstructure were investigated via scanning electron microscopy (SEM) using a JEOL JSM-IT200 (JEOL Ltd., Tokyo, Japan) operated at an accelerating voltage of 15 kV. Elemental analysis and mapping were performed using an integrated energy-dispersive X-ray spectroscopy (EDS, JEOL Ltd., Tokyo, Japan) system to evaluate the spatial distribution of the active components. Prior to imaging, the samples were mounted on aluminum stubs and sputter-coated with a thin layer of gold to minimize charging effects and enhance image resolution.

2.2.2. Textural and Spectroscopic Analysis

The specific surface area and textural properties were determined via N_2 adsorption–desorption at 77 K using a BELSORP MAX instrument (MicrotracBEL Corp., Osaka, Japan). The Brunauer–Emmett–Teller (BET) surface area was calculated from adsorption data in the relative pressure (P/P_0) range of 0.05–0.30. Prior to analysis, all samples were degassed under vacuum at 300 °C for 3 h. Raman spectroscopy was performed on a PerkinElmer System 2000 spectrometer (PerkinElmer Inc., Waltham, MA, USA) using an Ar ion laser (λ = 514 nm) with an output power of 20 mW. The spectra were collected in the 200–1000 cm^{-1} range to evaluate structural defects and lattice oxygen species.

2.2.3. Temperature-Programmed and Thermogravimetric Analyses

The reduction behavior, surface basicity, and carbon deposition were evaluated using a BELCAT II instrument equipped with a thermal conductivity detector (TCD) (MicrotracBEL Corp., Osaka, Japan).

H_2-TPR: Approximately 50 mg of sample was pretreated under helium at 120 °C for 30 min, followed by heating from 50 to 1000 °C (10 °C min^{-1}) under a 10 vol.% H_2/Ar flow.

CO_2-TPD: Surface basicity was probed by monitoring CO_2 desorption up to 800 °C in an Ar flow after the initial adsorption of 10 vol.% CO_2.

O_2-TPO: For the spent catalysts, carbonaceous deposits were quantified by heating the samples from room temperature to 900 °C (10 °C min^{-1}) under a 10 vol.% $O2/N_2$ flow. Before measurement, the samples were purged in situ with N_2 at 300 °C.

Thermogravimetric analysis (TGA) of the spent catalysts was carried out on a PerkinElmer TGA/DTA 6300 (SII NanoTechnology Inc., Tokyo, Japan). The samples were heated from ambient temperature to 1000 °C at a ramp rate of 20 °C/min under an air flow (100 mL/min) to determine the total weight loss and identify the types of carbon deposits formed during the reaction.

2.3. Catalytic Activity Measurements

2.3.1. Reactor Setup and Reaction Conditions

The partial oxidation of methane (POM) for hydrogen production was evaluated under atmospheric pressure in a continuous-flow, fixed-bed quartz reactor (5 mm ID, 500 mm length). In a typical run, 0.10 g of catalyst (sieved to 0.30–0.60 mm) was loaded into the reactor, secured between two layers of quartz wool. To ensure an isothermal catalyst bed and suppress axial temperature gradients, the catalyst was diluted with inert quartz sand (ratio 1:2 *w*/*w*) of similar granulometry. High-purity reactant gases (CH_4: 99.999%, O_2: 99.995%, and Ar: 99.995%) were regulated via mass flow controllers (MFCs).

2.3.2. Catalyst Pretreatment and Catalytic Testing

Prior to the catalytic test, the sample was reduced in situ at 400 °C for 2 h under a 30 vol.% H_2/Ar flow, followed by an Ar purge to remove residual hydrogen. The reaction was initiated by introducing a feed gas mixture with a molar ratio of $CH_4/O_2/Ar = 2/1/7$

(total flow rate: 100 mL min^{-1}). This setup corresponded to a gas hourly space velocity (GHSV) of approximately 40,000 h^{-1}, based on the total bed volume (V_{cat} = 0.15 cm^3). Catalytic performance was systematically investigated over a temperature range of 400–650 °C.

2.3.3. Product Analysis and Performance Metrics

The effluent gas composition was analyzed online using a Shimadzu GC-2014 gas chromatograph (Shimadzu Corporation, Kyoto, Japan) equipped with both a thermal conductivity detector (TCD) and a flame ionization detector (FID). Chromatographic separation of H_2, CO, CO_2, O_2, and unreacted CH_4 was achieved using a 60/80 Carboxen-1000 packed column (15 ft × 1/8 in). The column temperature was programmed from 35 to 220 °C to ensure optimal separation. The catalytic performance was quantified based on methane conversion and hydrogen yield, calculated as follows:

$$\% \text{ Conversion of methane} = \frac{CH_4in - CH_4out}{CH_4in} \times 100$$

$$\% \text{ Yield of hydrogen} = \frac{H_2out}{CH_4in \times 2} \times 100$$

3. Results and Discussion

The XRD patterns of the commercial GDC support and the Ni- and Cu-based catalysts are shown in Figure 1. All diffraction peaks can be indexed to the fluorite cubic structure of CeO_2 (JCPDS No. 43-1002), indicating that the crystal structure of the GDC support remains unchanged after metal impregnation and calcination. No additional diffraction peaks associated with crystalline impurity phases were observed in the GDC support, confirming the phase purity of the commercial material. Upon Cu loading, additional diffraction peaks appear at 2θ values of approximately 35.3° and 38.5°, which can be assigned to monoclinic CuO (JCPDS No. 05-0661). Similarly, Ni-loaded catalysts exhibit diffraction peaks at around 37.3° and 43.4°, characteristic of NiO (JCPDS No. 47-1049). These reflections indicate the presence of crystalline NiO and CuO phases on the GDC surface following calcination at 650 °C. In contrast, no distinct diffraction peaks attributable to rhenium oxide species (e.g., ReO_3 or Re_2O_7) were detected in the Re-containing catalysts because of the low Re loading (1 wt%), whose weak diffraction signals are likely masked by the intense reflections of the GDC support.

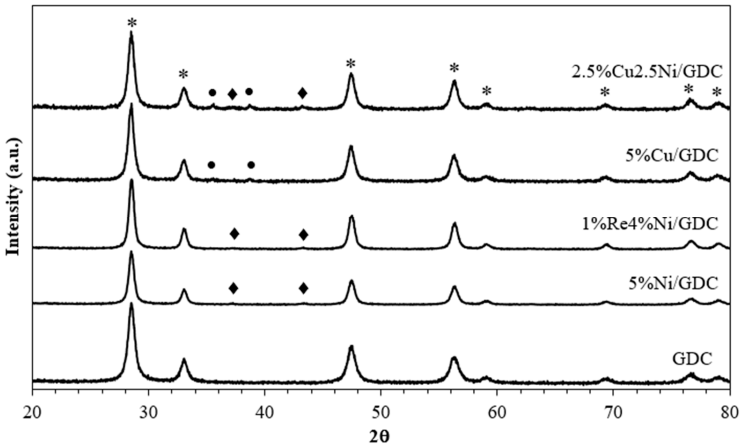


Figure 1. XRD patterns of commercial GDC support and supported catalysts after calcination at 650 °C. Diffraction peaks corresponding to * CeO_2 fluorite structure (JCPDS No. 43-1002), ♦ NiO (JCPDS No. 47-1049), and • CuO (JCPDS No. 05-0661) are indicated. The expected positions of rhenium oxide (ReO_x) reflections (e.g., ReO_3, JCPDS No. 40-1155) are marked for reference; however, no distinct ReO_x peaks are detected.

The N_2 adsorption–desorption isotherms for the GDC support and the modified Ni- and Cu-based catalysts are depicted in Figure 2, where all samples exhibit IUPAC Type IV isotherms featuring H_3-type hysteresis loops, confirming a mesoporous architecture characterized by slit-shaped interparticle voids within the GDC-metal framework [16]. The corresponding textural properties, including BET surface areas (S_{BET}) and crystallite sizes, are summarized in Table 1. The bare GDC support demonstrates a specific surface area of 85.5 m^2/g with a CeO_2 crystallite size of 12.3 nm. Following the impregnation of Ni and Cu and subsequent calcination at 650 °C, a significant reduction in S_{BET} to 37.9–45.6 m^2/g is observed. This loss in surface area is strongly correlated with the structural changes identified via XRD analysis, which revealed that the calcination process promoted the thermally induced growth of CeO_2 crystallites to 13.5–14.8 nm due to crystallite coalescence. Furthermore, XRD patterns confirmed the presence of crystalline NiO (at 37.3° and 43.4°) and CuO (at 35.3° and 38.5°) phases on the GDC surface. The deposition of these metal oxide crystallites further accounts for the decrease in S_{BET} through the partial blockage of the support's pore network and the inherently higher density of these metallic phases compared to the GDC support. Interestingly, despite the overall reduction in surface area after metal loading, the 3.5%Ni1.5%Cu/GDC catalyst maintained a relatively stable S_{BET} of 41.2 m^2/g and exhibited the highest adsorption volume among the modified samples, suggesting that the optimized Ni–Cu composition preserves a more accessible mesoporous architecture. In contrast, increasing the Cu loading (2.5%Ni2.5%Cu/GDC) resulted in the largest CeO_2 crystallite size (14.7 nm) and the lowest S_{BET} (37.9 m^2/g), indicating more pronounced pore blockage and crystallite growth.

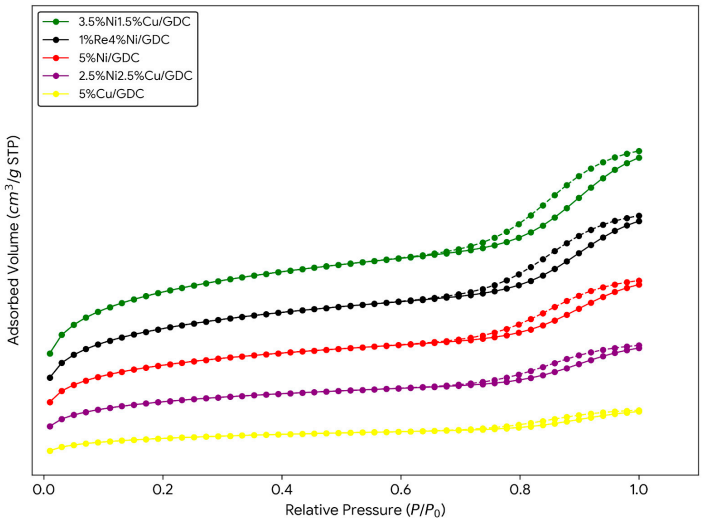


Figure 2. N_2 adsorption–desorption isotherms of the GDC-supported Ni and Cu catalysts.

Table 1. BET surface areas and crystallite sizes of supported Ni and Cu catalysts.

Catalysts	S_{BET} [a], m^2/g	Crystallite Size [b] (nm)	I_{570}/I_{460} [c]
GDC	85.5	12.3	0.41
5%Ni/GDC	40.2	14.8	0.06
5%Cu/GDC	45.6	14.2	0.27
4%Ni1%Re/GDC	43.7	13.5	0.25
2.5%Cu2.5%Ni/GDC	37.9	14.7	0.05
1.5%Cu3.5%Ni/GDC	41.2	13.8	0.42

[a] Estimated from N_2 adsorption at 77 K. [b] Calculated from the (111) crystallographic plan. [c] Estimated from Raman spectroscopy.

The SEM micrographs of 5%Ni/GDC, 5%Cu/GDC and 3.5%Ni–1.5%Cu/GDC (Figure 3) reveal noticeable differences in surface morphology and particle aggregation at 10,000× magnification. For 5%Ni/GDC, the surface appears rough and irregular, composed of unevenly sized particles that tend to form agglomerated clusters. This suggests that Ni particles are not uniformly distributed across the GDC surface. In contrast, the 5%Cu/GDC sample exhibits a comparatively smoother texture, with smaller, plate-like crystallites and reduced particle agglomeration, indicating a more uniform dispersion of Cu species. Meanwhile, the 3.5%Ni–1.5%Cu/GDC catalyst shows a relatively fine and homogeneous surface morphology. The particle boundaries appear less pronounced, and no distinct aggregation regions are observed, implying a more even particle distribution throughout the GDC support. Overall, the observed morphological variation suggests that introducing Cu tends to refine particle texture and enhance overall surface uniformity relative to Ni-only samples.

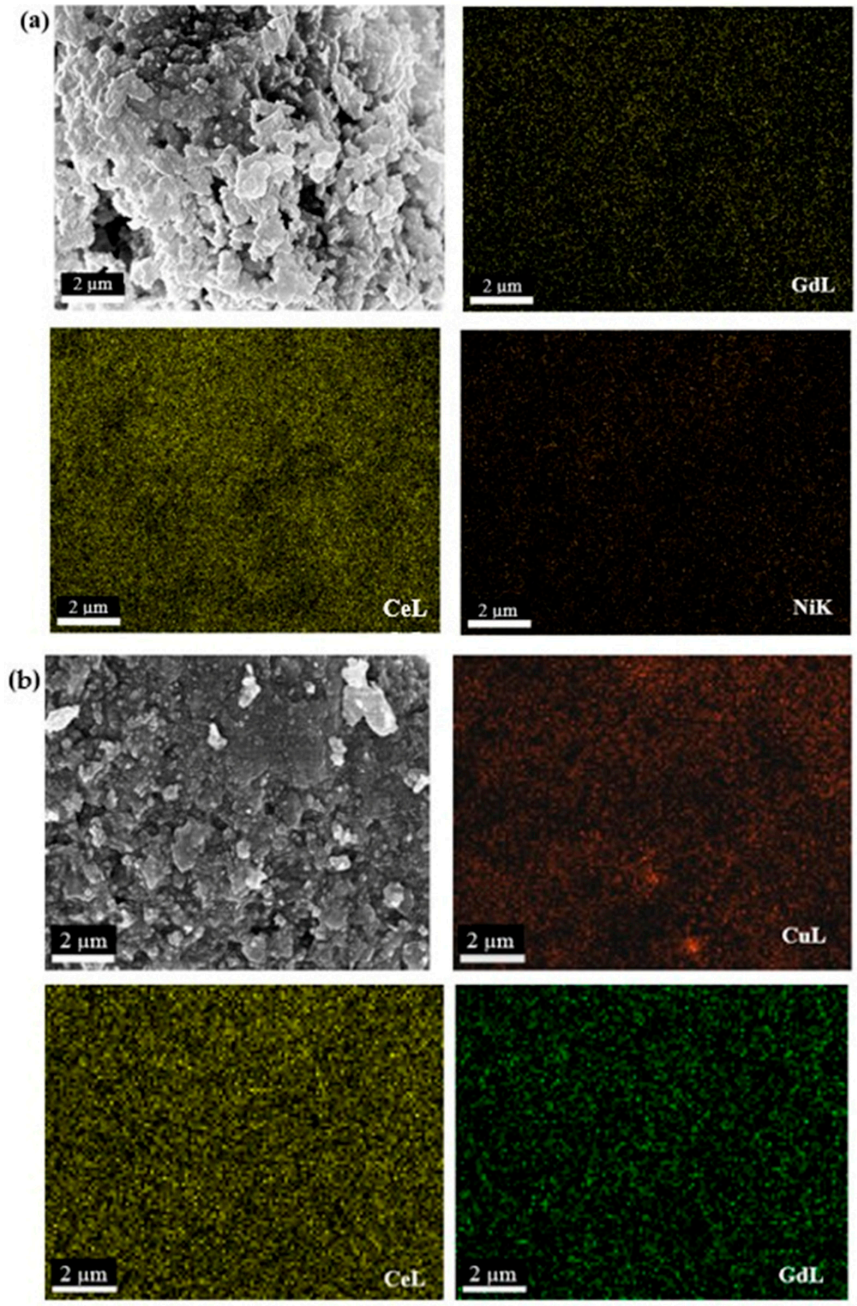


Figure 3. *Cont.*

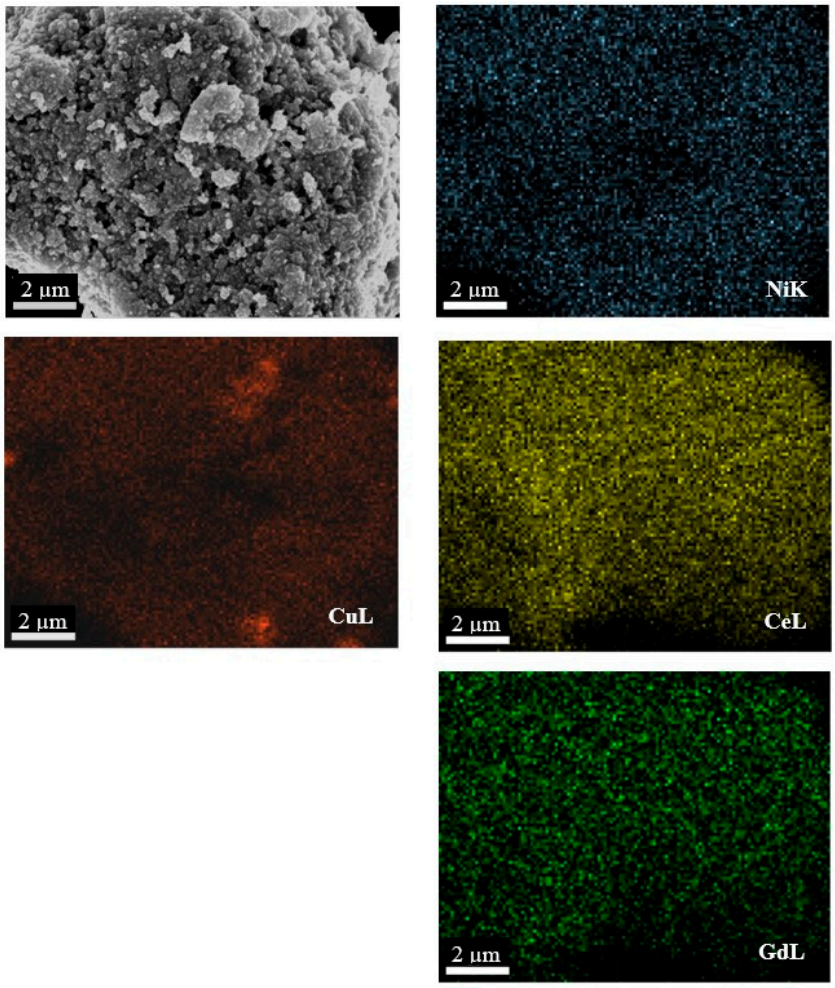


Figure 3. SEM pictures and elemental mapping of 5%Ni/GDC (**a**), 5%Cu/GDC (**b**) and 3.5%Ni 1.5%Cu/GDC (**c**) (10,000× magnification).

Elemental mapping images were obtained to confirm the spatial distribution of active metals (Ni, Cu) and the support elements (Ce, Gd) for each catalyst (Figure 3). In 5%Ni/GDC (Figure 3a), the elemental maps of Ni (NiK), Ce (CeL) and Gd (GdL) display a uniform signal intensity across the entire surface, suggesting that Ni species are evenly distributed and well dispersed on the GDC matrix without obvious localized enrichment. For 5%Cu/GDC (Figure 3b), the distribution maps of Cu (CuL), Ce (CeL) and Gd (GdL) show homogeneous elemental dispersion. No visible Cu clusters or phase segregation are detected, indicating that Cu species are well spread across the GDC surface and that the structural integrity of the support remains preserved. In the 3.5%Ni–1.5%Cu/GDC (Figure 3c) catalyst, the mapping results for Ni (NiK), Cu (CuL), Ce (CeL) and Gd (GdL) reveal that both Ni and Cu are distributed uniformly throughout the sample. The absence of distinct intensity variations or isolated bright spots suggests co-dispersion of the two metals on the GDC support. These observations confirm that the introduction of both Ni and Cu leads to a more homogeneous surface composition compared to the monometallic samples.

Figure 4 shows the Raman spectra of GDC supported mono- and bimetallic Ni- and Cu-based catalysts recorded in the range of 300–1000 cm^{-1}. All samples exhibit a dominant Raman band centered at approximately 460 cm^{-1}, corresponding to the F_{2g} vibrational mode of fluorite-structured CeO_2. This confirms that the cubic fluorite lattice of GDC remains structurally intact after metal incorporation. No additional Raman features associated with secondary cerium oxide phases were detected, indicating good structural stability of the support. A broad defect-related band in the range of 570–600 cm^{-1} is observed for

all samples, which is commonly attributed to oxygen vacancies, lattice distortions, and the presence of reduced Ce^{3+} species [17]. The intensity ratio of this defect band to the F_2g mode (I_{570}/I_{460}) was employed as a semi-quantitative descriptor of Raman-active oxygen vacancies [18] and the obtained values are summarized in Table 1. The bare GDC support exhibits a relatively high I_{570}/I_{460} ratio of 0.41, indicating a significant concentration of intrinsic oxygen vacancies associated with the doped ceria lattice. Upon metal loading, the Raman features are markedly modified, reflecting strong metal–support interactions and changes in the defect chemistry of GDC. For the monometallic 5%Ni/GDC catalyst, the defect-related band is strongly suppressed, resulting in a very low I_{570}/I_{460} ratio of 0.06. This pronounced decrease suggests that Ni incorporation leads to either vacancy delocalization or electronic screening of Raman-active defects, likely due to strong Ni–CeO_2 interactions and enhanced reducibility of the support [19]. A similar suppression is observed for the 2.5%Cu–2.5%Ni/GDC catalyst, which exhibits the lowest I_{570}/I_{460} ratio (0.05). This behavior implies that the balanced Ni–Cu composition effectively stabilizes the fluorite lattice and minimizes detectable oxygen vacancy signatures, possibly through electronic compensation effects or the formation of highly dispersed bimetallic species. In contrast, the 5%Cu/GDC catalyst displays a higher I_{570}/I_{460} ratio of 0.27, indicating that Cu incorporation induces a greater degree of lattice distortion and oxygen vacancy formation compared to Ni. This can be attributed to the weaker redox interaction between Cu species and ceria, which favors the generation of localized defects rather than their delocalization [20]. However, despite the higher defect signal, Cu/GDC shows inferior catalytic performance, suggesting that oxygen vacancies alone are insufficient to promote efficient methane activation in the absence of highly active metal sites. The bimetallic 4%Ni–1%Re/GDC catalyst exhibits an intermediate I_{570}/I_{460} value of 0.25. The presence of Re is known to enhance metal dispersion and stabilize the ceria lattice through strong electronic and redox interactions [21]. As a result, oxygen vacancy formation is moderated rather than maximized, leading to a controlled defect environment that balances lattice stability with oxygen mobility. Notably, the Ni-rich bimetallic 1.5%Cu–3.5%Ni/GDC catalyst shows the highest I_{570}/I_{460} ratio (0.42), exceeding even that of bare GDC. This indicates a synergistic effect between Ni and Cu in promoting the formation of Raman-active oxygen vacancies [22]. The combination of Ni-induced redox activity and Cu-induced lattice strain appears to facilitate vacancy generation and stabilization within the GDC lattice. Such a high concentration of oxygen vacancies is expected to enhance oxygen mobility and improve resistance to carbon accumulation under reaction conditions.

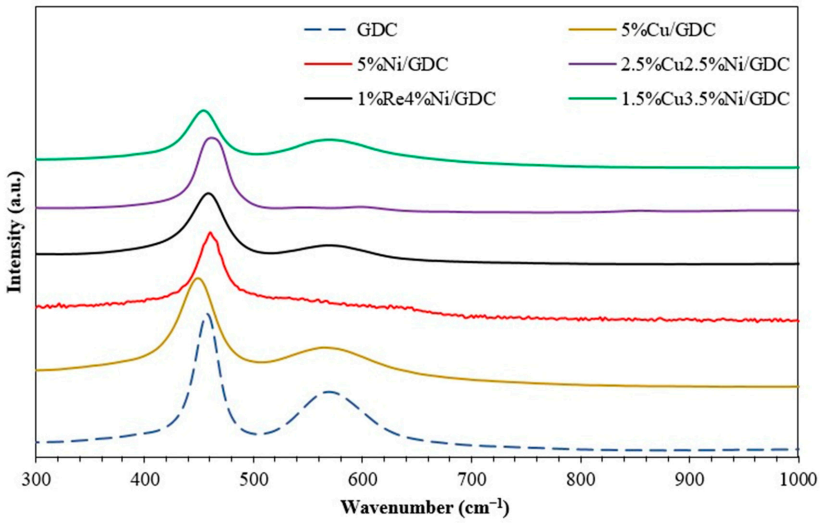


Figure 4. Raman spectra of Ni catalysts.

Figure 5 presents the H_2-TPR profiles of GDC-supported mono- and bimetallic Ni-, Cu-, and Re-based catalysts, providing insight into the reducibility of metal species and metal–support interactions. The bare GDC support exhibits a broad and weak reduction feature above 500 °C, which is attributed to the reduction of surface and subsurface oxygen species of CeO_2, consistent with the high oxygen storage capacity of doped ceria [23,24]. For the monometallic 5%Ni/GDC catalyst, a distinct reduction peak appears in the temperature range of 300–400 °C. This peak is assigned to the reduction of NiO species interacting with the GDC support. The relatively low reduction temperature indicates strong metal–support interactions and high reducibility of Ni species, which are favorable for methane activation during partial oxidation of methane (POM). In contrast, the 5%Cu/GDC catalyst displays reduction peaks at lower temperatures, typically below 250 °C, corresponding to the stepwise reduction of CuO to Cu^0. Despite the facile reducibility of Cu species, the absence of significant high-temperature reduction features suggests weak interaction with the ceria lattice [20]. The 1%Re/GDC catalyst shows a minor reduction feature at relatively high temperatures, reflecting the high dispersion and low reducibility of ReOx species. The presence of Re alone does not significantly enhance hydrogen consumption, indicating its limited direct contribution to methane activation. For the bimetallic 4%Ni–1%Re/GDC catalyst, the main NiO reduction peak shifts to lower temperatures compared to monometallic Ni/GDC. This shift indicates that Re acts as a promoter, facilitating hydrogen spillover and enhancing the reducibility of Ni species. Additionally, the reduction profile becomes narrower, suggesting improved dispersion of Ni particles and more uniform metal–support interactions [21]. The 2.5%Cu–2.5%Ni/GDC catalyst exhibits multiple overlapping reduction peaks, reflecting the coexistence of NiO and CuO species with different degrees of interaction with the GDC support. Notably, the reduction of Ni species occurs at lower temperatures than in monometallic Ni/GDC, implying a synergistic effect between Ni and Cu. The presence of Cu promotes hydrogen activation and accelerates the reduction of adjacent NiO species through hydrogen spillover [22]. The Ni-rich bimetallic 1.5%Cu–3.5%Ni/GDC catalyst shows the most pronounced low-temperature reduction behavior among all Ni-containing samples. The main reduction peak is shifted further toward lower temperatures, indicating enhanced reducibility of Ni species due to strong Ni–Cu interactions and improved metal dispersion. This enhanced reducibility is consistent with the higher concentration of oxygen vacancies observed in Raman analysis.

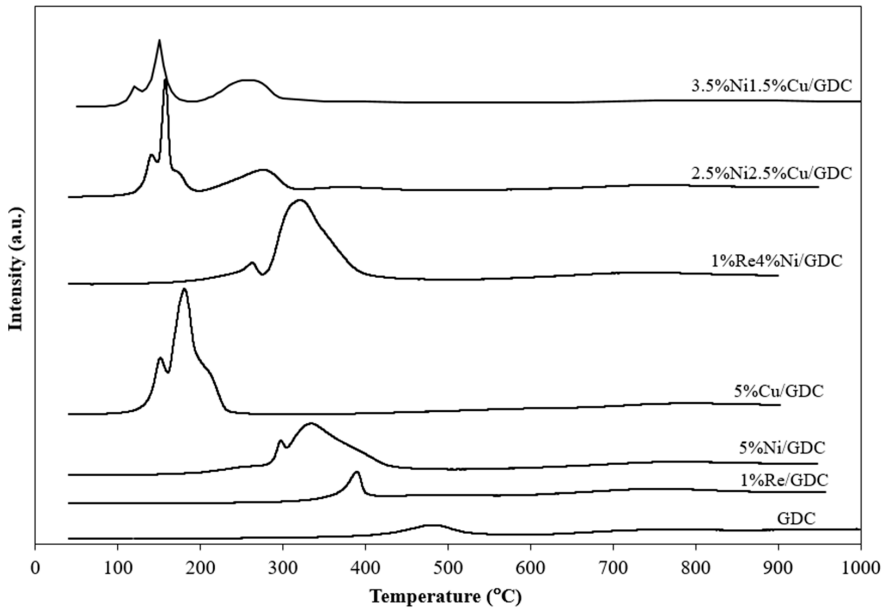


Figure 5. H_2-TPR profiles of GDC support, Ni- and Cu-based catalysts.

The formation of synthesis gas directly from methane in the presence of oxygen is commonly referred to as the direct partial oxidation of methane (POM) pathway [10]. Alternatively, syngas can be produced via an indirect POM pathway, in which methane first undergoes total oxidation (TOM; $CH_4 + 2O_2 \longrightarrow CO_2 + 2H_2O$), followed by subsequent reforming reactions, including dry reforming of methane (DRM; $CH_4 + CO_2 \longrightarrow 2CO + 2H_2$) and/or steam reforming of methane (SRM; $CH_4 + H_2O \longrightarrow CO + 3H_2$). In the indirect POM route, predominance of the SRM reaction over DRM leads to an increase in the H_2/CO ratio, allowing values greater than two to be achieved. Furthermore, the involvement of the water–gas shift (WGS) reaction ($CO + H_2O \longrightarrow CO_2 + H_2$) further enhances hydrogen production at the expense of CO, resulting in hydrogen-rich syngas [10,25].

The CO_2-TPD profiles of reduced mono- and bimetallic Ni- and Cu-based catalysts supported on GDC are presented in Figure 6, providing insights into the surface basicity and CO_2 adsorption strength of the catalysts. The desorption profiles can be divided into three temperature regions: low-temperature (<250 °C), medium-temperature (250–500 °C), and high-temperature (>500 °C) regions, corresponding to weak, moderate, and strong basic sites, respectively [26]. The monometallic 5%Cu/GDC catalyst exhibits relatively weak CO_2 desorption signals, with a dominant low-temperature peak below 250 °C and minimal contribution at higher temperatures. This behavior indicates the presence of mainly weak basic sites associated with surface hydroxyl groups or weakly bound carbonate species on Cu-modified ceria. The scarcity of medium- and high-temperature desorption features suggests limited strong CO_2 adsorption capability, which is consistent with the poor CO_2 activation and inferior syngas formation performance of Cu-based catalysts [27]. In contrast, the 5%Ni/GDC catalyst displays broader and more intense CO_2 desorption features extending into the medium- and high-temperature regions. The presence of a pronounced desorption peak above 500 °C indicates the formation of strong basic sites. These strong basic sites enhance CO_2 adsorption and activation, facilitating carbon removal through surface oxidation pathways during methane partial oxidation [28]. The incorporation of Re as a promoter in the 4%Ni–1%Re/GDC catalyst leads to a noticeable increase in CO_2 desorption intensity across the medium-temperature region. This suggests that Re promotes the formation of moderately strong basic sites by enhancing metal dispersion and stabilizing interfacial Ni–CeO_2 sites. The balanced distribution of basic sites is favorable for CO_2 activation while avoiding excessive strong adsorption that could hinder desorption kinetics. Bimetallic Ni–Cu catalysts exhibit distinct CO_2-TPD behaviors depending on composition. The 2.5%Ni–2.5%Cu/GDC catalyst shows enhanced CO_2 desorption in the medium-temperature range compared to monometallic Cu/GDC, indicating synergistic effects between Ni and Cu in generating accessible basic sites. However, the high-temperature desorption intensity remains moderate, suggesting limited formation of excessively strong basic sites. Notably, the Ni-rich 3.5%Ni–1.5%Cu/GDC catalyst exhibits the strongest overall CO_2 desorption, particularly in the high-temperature region above 600 °C. This indicates a high density of strong basic sites, likely associated with abundant oxygen vacancies and Ni–Cu–Ce interfacial structures. Such strong CO_2 adsorption is beneficial for gasifying surface carbon species and enhancing catalyst stability under POM conditions [22].

The nature and reactivity of the carbonaceous deposits on the spent catalysts were investigated using O_2-TPO (Figure 7). The profiles reveal distinct oxidation features that vary significantly with the metal composition. In the O_2-TPO profiles, oxidation peaks observed at low (~300 °C) and intermediate (400–500 °C) temperatures are attributed to highly reactive carbon species (C_α) and less reactive carbon species (C_β), respectively [29]. These carbon species are generally associated with amorphous carbon deposits [30]. In contrast, oxidation peaks appearing at high temperatures (~800 °C) are indicative of inert carbon species, commonly referred to as graphitic carbon, which is known to be detrimental to catalytic

performance due to its resistance to oxidation and its tendency to block active sites. The 2.5%Ni2.5%Cu/GDC and 5%Ni/GDC catalysts show a dominant oxidation peak centered around 250–260 °C, which is attributed to the combustion of highly reactive amorphous carbon species. Notably, the 2.5%Ni2.5%Cu/GDC catalyst also exhibits a secondary broad shoulder extending towards 500 °C, suggesting a higher degree of carbon accumulation or the formation of more ordered carbon structures compared to others. Interestingly, the 3.5%Ni1.5%Cu/GDC and 5%Cu/GDC samples display significantly lower intensities in the TPO profiles. For 3.5%Ni1.5%Cu/GDC, this correlates well with the Raman analysis, where a high concentration of oxygen vacancies was observed. These vacancies facilitate oxygen mobility from the GDC lattice to the metal-support interface, promoting the continuous gasification of carbon precursors and thus suppressing coke buildup. To quantify the amount of carbon deposited during the reaction, TGA was performed (Figure 8). The total weight loss follows the order: 2.5%Ni2.5%Cu/GDC (6.6%) > 5%Ni/GDC (3.3%) > 4%Ni1%Re/GDC (2.9%) > 3.5%Ni1.5%Cu/GDC (2.2%)~5%Cu/GDC (2.0%). The 2.5%Ni2.5%Cu/GDC catalyst suffered the most significant weight loss, indicating that an equal ratio of Ni and Cu may lead to larger alloy particles or reduced oxygen mobility, hindering carbon gasification [31]. Whereas the 5%Cu/GDC catalyst exhibited the lowest carbon accumulation among the tested samples, as evidenced by the minimal weight loss (~2.0%) in TGA and the negligible oxidation features in O_2-TPO. However, this low coking rate is not indicative of superior stability but rather reflects the poor catalytic activity of Cu-species for methane activation. The CO_2-TPD profiles further reveal a lack of strong basic sites on the Cu/GDC surface, hindering the essential gasification pathways. Combined with the weak metal-support interactions observed in H_2-TPR, it can be concluded that monometallic Cu lacks the necessary redox and electronic properties to facilitate efficient syngas production compared to its Ni-based counterparts. In contrast, the 3.5%Ni1.5%Cu/GDC catalyst demonstrated superior coking resistance. This result highlights the synergistic effect of the Ni-rich bimetallic composition, where the presence of a specific amount of Cu (1.5%) enhances Ni dispersion and increases Raman-active oxygen vacancies, effectively balancing the rate of methane activation and carbon removal.

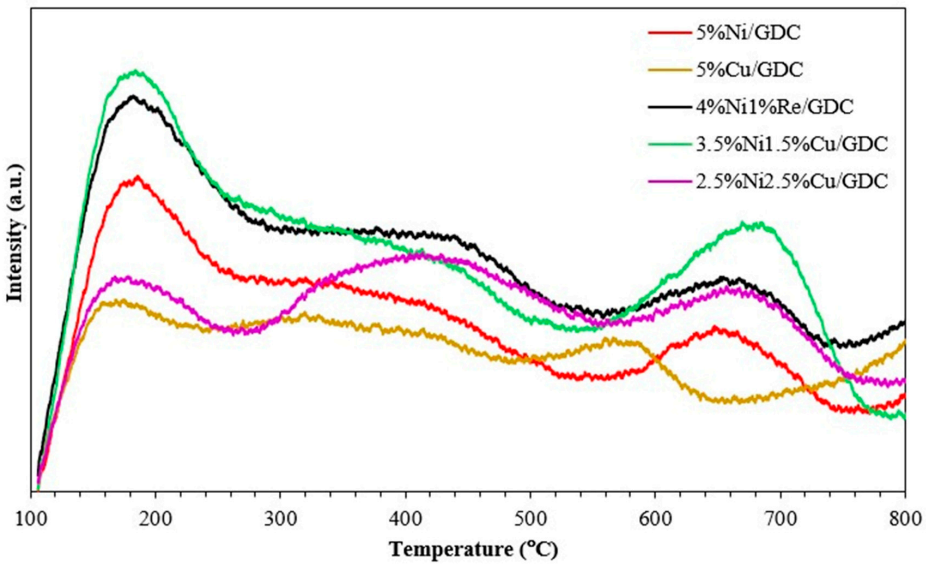


Figure 6. CO_2-TPD of reduced Cu- and Ni-based catalysts.

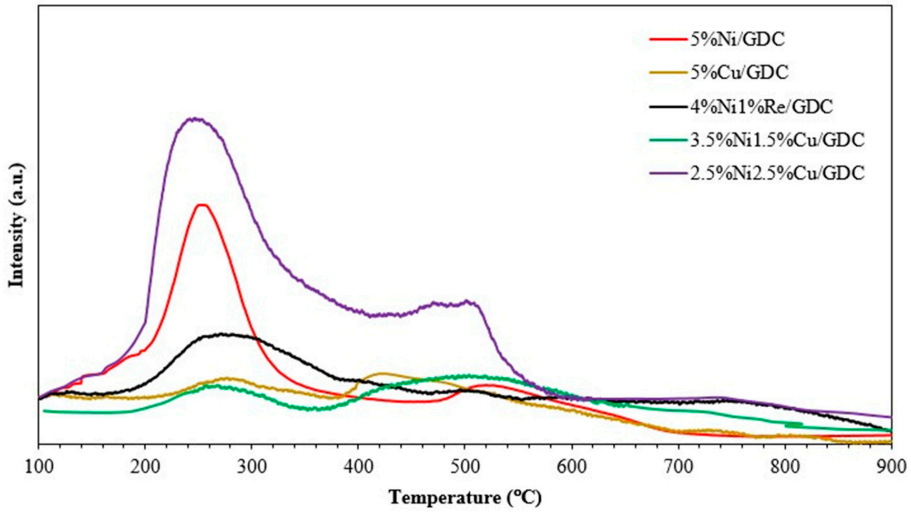


Figure 7. O_2-temperature-programmed oxidation of the used Ni catalysts.

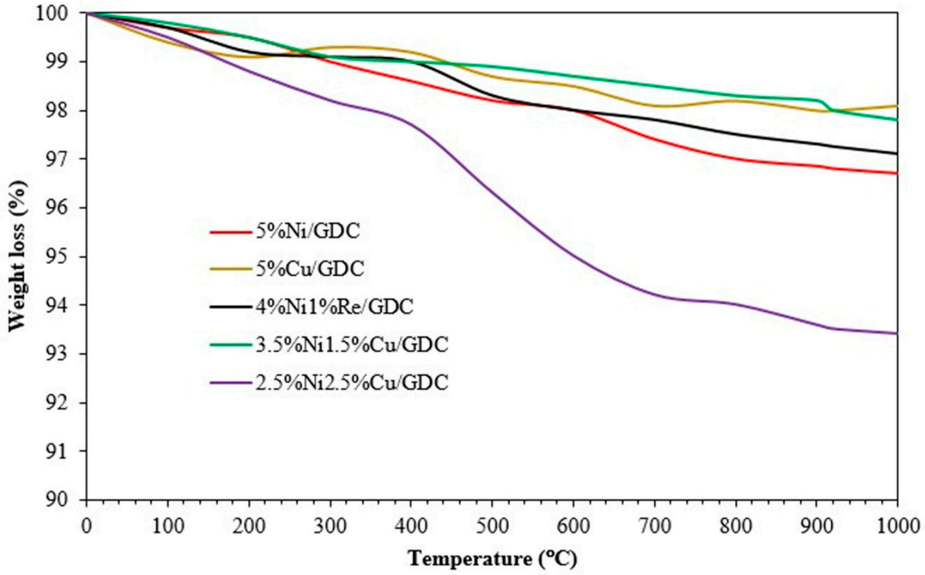


Figure 8. Thermogravimetry analysis of the used Ni catalysts.

The structural evolution and carbon deposition characteristics of the spent catalysts were further scrutinized using Raman spectroscopy (Figure 9). Two distinct bands observed at ~1350 cm^{-1} (D-band) and ~1580^{-1} (G-band) correspond to the A_{1g} breathing mode of disordered carbon and the E_{2g} stretching mode of sp^2 hybridized graphitic carbon, respectively. The 3.5%Ni–1.5%Cu/GDC catalyst exhibited significantly lower D and G band intensities compared to other samples. Crucially, the absence of a sharp, intense G-band confirms that this specific Ni/Cu ratio effectively suppresses the formation of inert, graphitic carbon. This result is in excellent agreement with TPO data, which showed no high-temperature oxidation peaks for this sample. In contrast, the 2.5%Cu–2.5%Ni/GDC sample displayed the most intense carbon signals, correlating with the highest weight loss (6.6%) observed in TGA. This indicates that an equal ratio of Ni and Cu may lead to larger metal ensembles or reduced metal-support interaction, which accelerates carbon nucleation. While the 1%Re–4%Ni/GDC, 5%Ni/GDC and 5%Cu/GDC catalysts showed moderate carbon bands, their G-band intensities were noticeably higher than the 3.5%Ni–1.5%Cu/GDC catalyst, suggesting a higher degree of carbon crystallinity (graphitization) which can lead to long-term deactivation. In summary, the Raman analysis reveals that the 3.5%Ni–1.5%Cu/GDC catalyst superior performance is twofold: (i) it preserves a high density of oxygen vacancies

(I_{570}), and (ii) it minimizes the formation of graphitic carbon. The integration of 1.5% Cu with 3.5% Ni optimizes the surface basicity and defect concentration, creating a surface environment where carbon precursors are oxidized more rapidly than they can polymerize into graphitic structures.

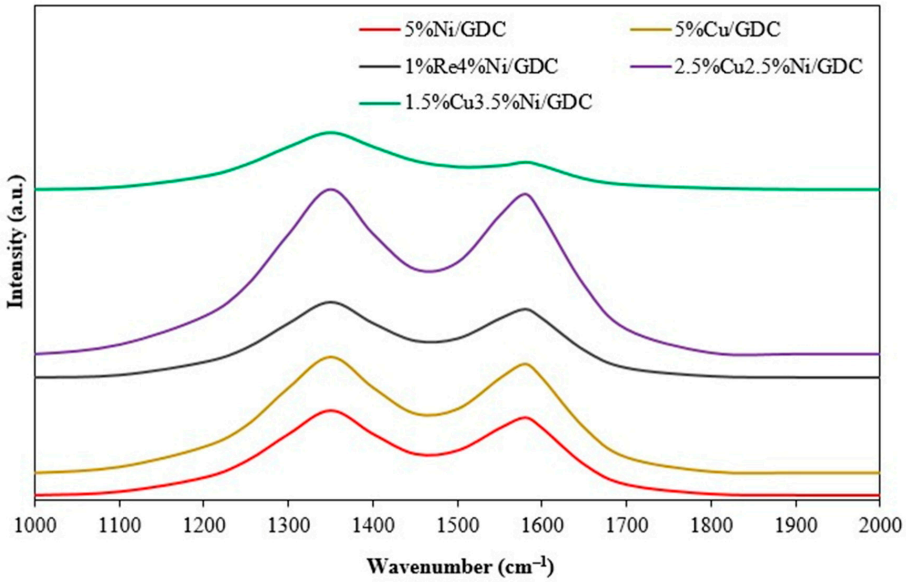


Figure 9. Raman spectra of the used catalysts after operating the POM reaction.

Blank experiments for the partial oxidation of methane were conducted in the temperature range of 600–650 °C to evaluate the contribution of non-catalytic reactions. At 600 °C, a low methane conversion of 2.5% was observed without any detectable syngas formation. Even at 650 °C, although methane conversion slightly increased to 4.3%, syngas was still not detected. These results clearly indicate that methane partial oxidation to syngas proceeds only in the presence of an active catalyst under the investigated conditions. The catalytic performances of the prepared catalysts in terms of CH_4 conversion, H_2 yield, and H_2/CO ratio are summarized in Figure 10a–d. The effect of reaction temperature on catalytic activity was systematically investigated over Ni- and Cu-based catalysts. For the Ni/GDC catalyst, increasing the reaction temperature from 400 to 650 °C led to a sharp increase in CH_4 conversion from 78% to complete conversion, accompanied by an increase in H_2 yield from 66% to 78%. Overall, Ni/GDC, NiRe/GDC, and NiCu/GDC catalysts exhibited significantly higher methane conversion and hydrogen yield compared to Cu/GDC catalysts, highlighting the superior methane activation capability of Ni-based systems. At 600 °C, the 5%Ni/GDC catalyst achieved 100% CH_4 conversion with a hydrogen yield of 75% and an H_2/CO ratio of 2.60. An H_2/CO ratio greater than 2 indicates that syngas formation proceeds predominantly through an indirect POM pathway, involving total oxidation of methane ($CH_4 + 2O_2 \longrightarrow CO_2 + 2H_2O$), followed by secondary reforming reactions such as dry reforming and steam reforming. Oxygen vacancies and surface basic sites act as adsorption and activation centers for CO_2 and H_2O, enabling their subsequent reaction with methane to form CO and H_2 [32,33]. In contrast, the Cu-only catalyst (5%Cu/GDC) showed a drastic decline in catalytic activity at 600 °C, with CH_4 conversion and H_2 yield dropping to 24% and 4%, respectively, indicating insufficient methane activation over Cu sites. Interestingly, the introduction of a small amount of Cu into the Ni-based system significantly altered the reaction selectivity. The 3.5%Ni1.5%Cu/GDC catalyst achieved a markedly higher H_2/CO ratio of 3.11 compared to 5%Ni/GDC, while maintaining high methane conversion. This enhancement suggests that hydrogen-producing and CO-consuming reactions, particularly the water–gas shift ($CO + H_2O \longrightarrow H_2 + CO_2$), are favored over

hydrogen-consuming reactions such as the reverse WGS under POM conditions. These reactions are expected to occur in parallel with POM within the same temperature window. To achieve the target of a high H_2/CO ratio combined with high methane conversion, the Ni–Cu composition was optimized by incorporating 1.5%Cu with 3.5%Ni on the GDC support. As evidenced by Raman and CO_2-TPD analyses, the 3.5%Ni1.5%Cu/GDC catalyst exhibits the highest concentration of oxygen vacancies and surface basic sites, which facilitate the adsorption and activation of CO_2 and H_2O generated during methane oxidation. These species subsequently participate in reforming reactions via the indirect POM route, thereby enhancing hydrogen production [34]. Additionally, the presence of Cu likely promotes WGS-like reactions, further increasing hydrogen yield and suppressing CO concentration. As a result, the 3.5%Ni–1.5%Cu/GDC catalyst achieved 95% CH_4 conversion, 84% H_2 yield, and an H_2/CO ratio of 3.11 at 600 °C, representing the best overall performance among the investigated catalysts. In contrast, the 2.5%Ni–2.5%Cu/GDC catalyst exhibited a lower population of oxygen vacancies and basic sites, along with increased carbon deposition, leading to inferior catalytic performance (87% CH_4 conversion, 68% H_2 yield, and an H_2/CO ratio of 2.55 at 600 °C). The long-term stability of the optimal 3.5%Ni–1.5%Cu/GDC catalyst was further evaluated over a 40 h time-on-stream test (Figure 10d). The catalyst maintained a stable H_2/CO ratio in the range of 3.05–3.15 throughout the entire testing period, demonstrating excellent catalytic stability and sustained hydrogen-rich syngas production under POM conditions.

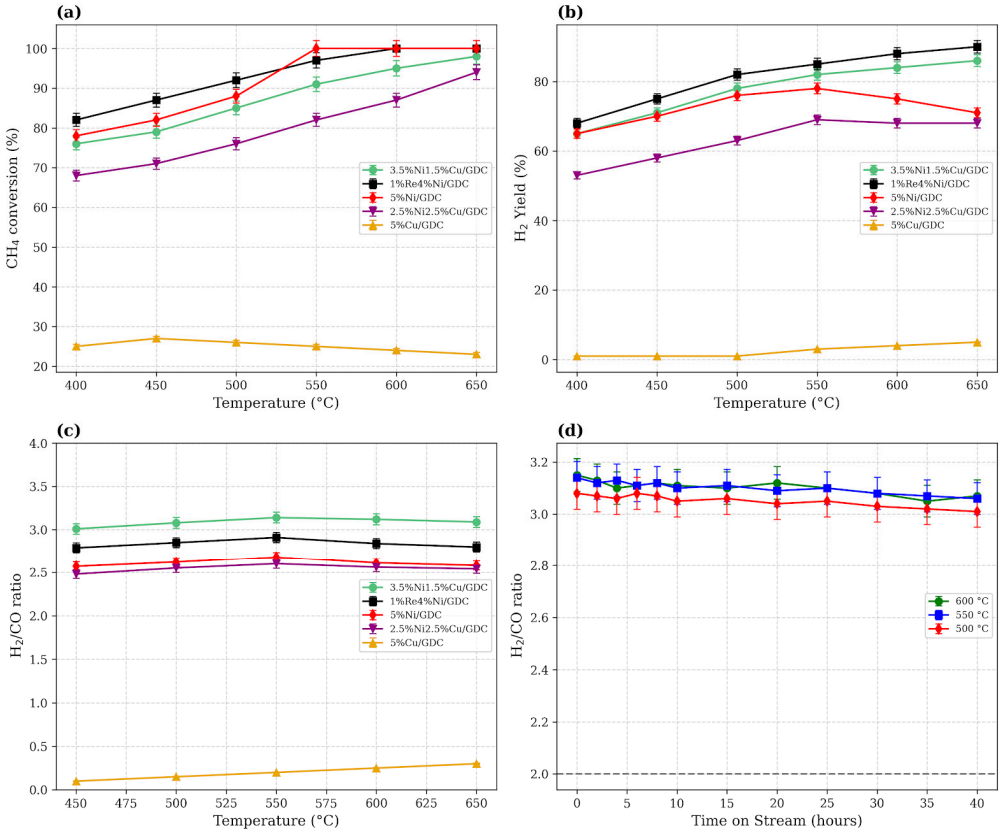


Figure 10. The catalytic activity results: (**a**) CH_4 conversion, (**b**) H_2 yield (%), (**c**) H_2/CO ratio and (**d**) long-term study of 3.5%Ni1.5%Cu/GDC at different temperatures.

The superior performance of the 3.5%Ni–1.5%Cu/GDC catalyst can be traced back to the "Ensemble Effect" and the "Electronic Effect" of the bimetallic architecture (Figure 11). According to the ensemble effect, the addition of a small amount of Cu (1.5%) effectively dilutes the surface Nickel clusters, breaking up large Ni ensembles that are responsible for

the cracking of methane into graphitic carbon. Smaller Ni clusters have been theoretically and experimentally shown to favor the formation of CO over graphitic carbon filaments. From an electronic perspective, the interaction between Ni and Cu atoms at the GDC interface modulates the d-band center of the active metal sites, optimizing the adsorption energy of methane fragments. This electronic tuning, combined with the hydrogen spillover effects observed in TPR, ensures that the metallic state of Ni is maintained under the oxidizing POM environment, preventing the formation of inactive Ni^{2+} ions [35,36].

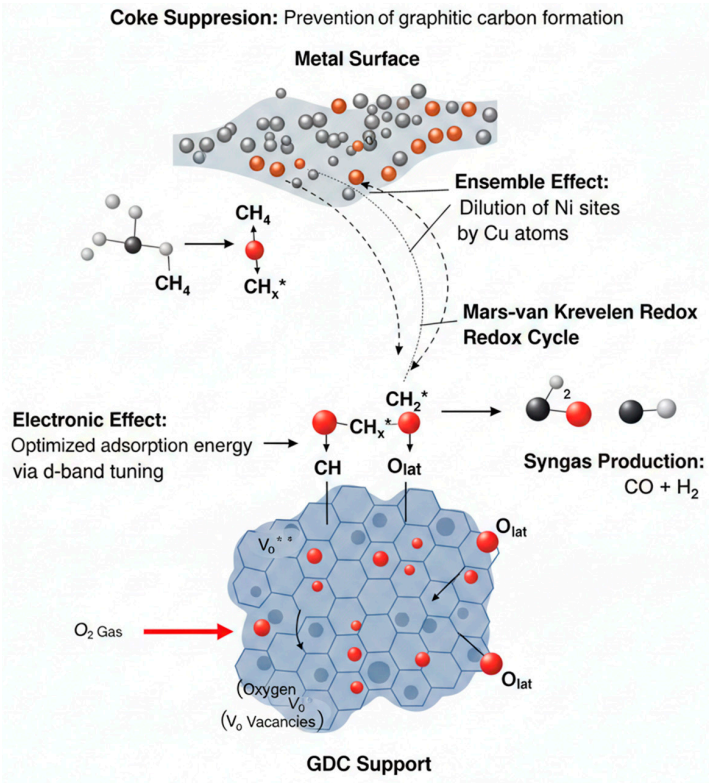


Figure 11. Schematic illustration of the synergistic reaction mechanism over the bimetallic Ni–Cu/GDC catalyst during the partial oxidation of methane (POM). Legend: The color coding for atoms is as follows: Grey = Ni, Orange = Cu, Black = C, White = H, and Red = O (Lattice and Gas-phase oxygen). The blue structure represents the GDC support lattice, with dark spots indicating oxygen vacancies (V_o). The asterisk (*) denotes surface-adsorbed species (e.g., CH_x^*). Solid black arrows trace the transformation of methane into syngas, while the dashed arrows illustrate the Mars-van Krevelen redox cycle interactions between the metal surface and the support. The red arrow indicates the replenishment of oxygen vacancies by gas-phase O_2.

The role of the GDC support is equally vital. The high concentration of intrinsic and extrinsic oxygen vacancies (I_{570}/I_{460} = 0.42) acts as an "oxygen reservoir". During the reaction, surface lattice oxygen reacts with adsorbed carbonaceous species (CH_x*) to form syngas, while gas-phase oxygen refills the vacancies, maintaining a continuous redox cycle. This cycle is significantly more efficient on GDC than on pure CeO_2 or CeO_2-ZrO_2 supports due to the enhanced ionic conductivity provided by Gadolinium doping [37].

The 3.5%Ni–1.5%Cu/GDC catalyst developed in this study exhibits a superior combination of activity and stability compared to several reported benchmarks (Table 2). Most notably, achieving 95% CH_4 conversion and 84% H_2 yield at 600 °C while remaining stable for 40 h is a significant technical achievement. In contrast, monometallic 5% Ni/CeO_2 has been reported to reach only 50% conversion at 600 °C and shows signs of deactivation over a shorter 15-h period. The incorporation of 1.5% Cu induces a pronounced synergistic effect, effectively doubling the methane conversion and substantially extending catalyst

lifetime. This enhancement is closely associated with optimized surface basicity and an increased density of oxygen vacancies. Furthermore, the transition metal bimetallics such as Ni-Ga/DSZ95 demonstrate high structural stability and resistance to sintering, however they often require higher operating temperatures (700 °C) to reach conversions that the 3.5/1.5 Ni-Cu catalyst achieves at 600 °C. When benchmarked against noble metal catalysts, the Ni-Cu/GDC system remains highly competitive. For example, while Rh/Al_2O_3 catalysts are known for excellent coke resistance at 800 °C, the GDC-supported system achieves high conversion levels (95%) at a much lower temperature (600 °C) without utilizing precious metals. Similarly, it outperforms Ru-promoted systems in terms of hydrogen yield (84% vs. 80% for $Ru-Ni/CeO_2$). This high low-temperature activity is vital for industrial applications as it reduces the thermal stress on reactor components and lowers energy consumption. Furthermore, the stability profile of the Ni-Cu/GDC catalyst is more robust than hydrotalcite-derived (HT) systems, which achieved only 48% yield over 15 h, and Sr-promoted systems that, while showing high initial yields, are often tested for shorter periods. The low TGA weight loss (2.2 wt%) after 40 h confirms that the GDC support successfully facilitates the continuous gasification of carbon filaments, a mechanism that is often missing in non-reducible supports like Al_2O_3 or MgO.

Table 2. Comparison of catalytic performance, coking behavior, and stability of the present catalyst with literature-reported systems.

Catalyst System	Support	T (°C)	X_{CH4}* (%)	H_2 Yield (%)	Stability/Coking	References
3.5%Ni–1.5%Cu	GDC	600	95.0	84.0	Stable 40 h/2.2 wt% coke	This Work
1%Ru–0.5%Ni	CeO_2	600	85.0	80.0 **	High stability/Low coke	[38]
5%Ni–2%Sr	MgO	600	86.3	84.0	Stable > 240 min/0.7 wt% coke	[39]
1.38%Ni–0.12%Pd	CeO_2	550	73.1	67.0 **	High stability (BM method)	[40]
5%Ni + 1%Ga	DSZ95	700	75.9	74.8	Stable 240 min/Low coke	[41]
5%Ni–HT-70	Mg-Al	600	52.0	46.0	Stable 15 h/Low coke	[42]
1.5%Rh	Al_2O_3	800	84.5	~50.0	Moderate coking	[43]
5%Ni	CeO_2	600	50.0	40.0	Deactivates within 15 h	[44]

X_{CH4}* is CH_4 Conversion (%), ** Syngas yield (H_2 + CO).

4. Conclusions

In conclusion, this study elucidates the critical role of Ni–Cu synergistic interactions and support defect chemistry in governing the catalytic behavior of Gd-doped CeO_2-supported bimetallic catalysts for the partial oxidation of methane. Among the investigated formulations, the 3.5%Ni–1.5%Cu/GDC catalyst emerges as a highly efficient and durable system, achieving a CH_4 conversion of 95% and an elevated H_2/CO ratio of 3.11 at 600 °C, while maintaining stable performance over 40 h on stream.

Comprehensive physicochemical characterization reveals that the superior activity and coke resistance of this catalyst originate from a combination of interconnected factors. Raman spectroscopy demonstrates that the optimized Ni–Cu composition maximizes the density of Raman-active oxygen vacancies, as reflected by the high I570/I460 ratio. This defect-rich structure enhances lattice oxygen mobility, enabling the continuous in situ gasification of carbonaceous intermediates and effectively suppressing their transformation into inactive graphitic species, as corroborated by O_2-TPO and TGA analyses.

Furthermore, the incorporation of Cu into the Ni/GDC system effectively modulates surface basicity and improves the reducibility of the active phases. These modifications promote the adsorption and activation of H_2O and CO_2 intermediates, thereby facilitating secondary reforming reactions and water–gas shift-like pathways. The contribution of

these reactions accounts for the enhanced hydrogen yield and the H_2/CO ratio exceeding the stoichiometric value expected for direct POM.

A clear structure–activity relationship is established between the Ni/Cu atomic ratio and the catalyst's ability to inhibit the formation of ordered carbon species. The Ni-rich bimetallic configuration provides an optimal balance between efficient Ni-centered methane activation and Cu-induced tuning of surface and electronic properties, resulting in high syngas selectivity while preserving structural integrity under reaction conditions.

Funding: This study was supported by Thammasat University Research Fund, Contract No. TUFT 018/2568.

Data Availability Statement: The original contributions presented in this study are included in the article. Further inquiries can be directed to the author.

Conflicts of Interest: The author declares no conflicts of interest.

References

1. Holmen, A. Direct conversion of methane to fuels and chemicals. *Catal. Today* **2009**, *142*, 2–8. [CrossRef]
2. Osman, A.I. Catalytic hydrogen production from methane partial oxidation: Mechanism and kinetic study. *Chem. Eng. Technol.* **2020**, *43*, 641–648. [CrossRef]
3. Shi, Y.; Tian, X.; Deng, Z.; Shi, W.; Fan, W.; Wang, F. Review and outlook of confined Ni catalysts for the dry reforming of methane reaction. *Energy Fuels* **2024**, *38*, 1633–1656. [CrossRef]
4. Usman, M.; Wan Daud, W.M.A.; Abbas, H.F. Dry reforming of methane: Influence of process parameters—A review. *Renew. Sustain. Energy Rev.* **2015**, *45*, 710–744. [CrossRef]
5. Li, L.; Dostagir, N.H.M.D.; Shrotri, A.; Fukuoka, A.; Kobayashi, H. Partial oxidation of methane to syngas via formate intermediate found for a ruthenium–rhenium bimetallic catalyst. *ACS Catal.* **2021**, *11*, 3782–3789. [CrossRef]
6. Liu, H.; He, D. Recent progress on Ni-based catalysts in partial oxidation of methane to syngas. *Catal. Surv. Asia* **2012**, *16*, 53–61. [CrossRef]
7. Al-Fatesh, A.S.; Vadodariya, D.M.; Banabdwin, K.M.; Ibrahim, A.A.; Fakeeha, A.H.; Adil, S.F.; Kumar, R.; Abahussain, A.A.M. Promoted Ni catalyst over titania-zirconia support for partial oxidation of methane: Simple and practical catalysts. *Catal. Lett.* **2024**, *154*, 4625–4635. [CrossRef]
8. Choudhary, V.R.; Mondal, K.C.; Choudhary, T.V. Partial oxidation of methane to syngas with or without simultaneous steam or CO_2 reforming over a high- temperature stable-NiCoMgCeOx supported on zirconia–hafnia catalyst. *Appl. Catal. A* **2006**, *306*, 45–50. [CrossRef]
9. Fazlikeshteli, S.; Vendrell, X.; Llorca, J. Bimetallic Ru–Pd supported on CeO_2 for the catalytic partial oxidation of methane into syngas. *Fuel* **2023**, *334*, 126799. [CrossRef]
10. Luo, Z.; Kriz, D.A.; Miao, R.; Kuo, C.-H.; Zhong, W.; Guild, C.; He, J.; Willis, B.; Dang, Y.; Suib, S.L.; et al. TiO_2 Supported gold–palladium catalyst for effective syngas production from methane partial oxidation. *Appl. Catal. Gen.* **2018**, *554*, 54–63. [CrossRef]
11. Koh, A.C.W.; Chen, L.; Leong, W.K.; Johnson, B.F.G.; Khimyak, T.; Lin, J. Hydrogen or synthesis gas production via the partial oxidation of methane over supported nickel–cobalt catalysts. *Int. J. Hydrogen Energy* **2007**, *32*, 725–730. [CrossRef]
12. Salazar-Villalpando, M.D.; Reyes, B. Hydrogen production over Ni/ceria-supported catalysts by partial oxidation of methane. *Int. J. Hydrogen Energy* **2009**, *34*, 9723–9729. [CrossRef]
13. Lanza, R.; Velasco, J.A.; Jaras, S.G. Recent developments and achievements in partial oxidation of methane with and without addition of steam. *R. Soc. Chem.* **2001**, *23*, 50–95.
14. Tepamatr, P.; Laosiripojana, N.; Charojrochkul, S. Water gas shift reaction over monometallic and bimetallic catalysts supported by mixed oxide materials. *Appl. Catal. A Gen.* **2016**, *523*, 255–262. [CrossRef]
15. Tepamatr, P.; Buarod, E.; Laosiripojana, N.; Charojrochkul, S. Study of Water Gas Shift reaction over Ceria based Catalysts in Solid Oxide Fuel Cells. *Electrochem. Soc.* **2015**, *68*, 1207–1217.
16. Thommes, M.; Kaneko, K.; Neimark, A.V.; Olivier, J.P.; Rodriguez-Reinoso, F.; Rouquerol, J.; Sing, K.S.W. Physisorption of gases, with special reference to the evaluation of surface area and pore size distribution (IUPAC Technical Report). *Pure Appl. Chem.* **2015**, *87*, 1051–1069. [CrossRef]
17. Spanier, J.E.; Robinson, R.D.; Zhang, F.; Chan, S.-W.; Herman, I.P. Size-dependent properties of CeO_2 nanoparticles as studied by Raman scattering. *Phys. Rev. B* **2001**, *64*, 245407. [CrossRef]

18. Mukherjee, D.; Rao, B.G.; Reddy, B.M. Characterization of ceria-based nano-oxide catalysts by Raman Spectroscopy. *Top. Catal.* **2017**, *60*, 1673–1681. [CrossRef]
19. Rodriguez, J.A.; Hanson, J.C.; Chaturvedi, S.; Albornoz, A.; Brito, J.L. Structural and electronic properties of $Ce_{1-x}M_xO_{2-\gamma}$ (M = Ti, Zr, Hf): Fundamental understanding of the behavior of mixed-oxides. *J. Phys. Chem. B* **2002**, *106*, 765–773.
20. Liu, X.; Zhou, K.; Wang, L.; Wang, B.; Li, Y. Oxygen vacancy clusters promoting reducibility and activity of ceria nanorods. *J. Am. Chem. Soc.* **2009**, *131*, 3140–3141. [CrossRef] [PubMed]
21. Li, S.; Gong, J. Strategies for improving the performance and stability of Ni-based catalysts for reforming reactions. *Chem. Soc. Rev.* **2014**, *43*, 7245–7256. [CrossRef]
22. Liu, Z.; Grinter, D.C.; Lustemberg, P.G.; Nguyen-Phan, T.-D.; Zhou, Y.; Luo, S.; Waluyo, I.; Crumlin, E.J.; Stacchiola, D.J.; Zhou, J.; et al. Dry reforming of methane on a highly-active Ni-CeO_2 catalyst: Effects of metal-support interactions on C–H bond breaking. *Angew. Chem. Int. Ed.* **2016**, *55*, 7455–7459. [CrossRef]
23. Trovarelli, A. Catalytic properties of ceria and CeO_2-containing materials. *Catal. Rev.* **1996**, *38*, 439–520. [CrossRef]
24. Lomonaco, J.G.; Sesuk, T.; Charojrochkul, S.; Tepamatr, P. Effect of Re addition on the water–gas shift activity of Ni catalyst supported by mixed oxide materials for H_2 production. *Catalysts* **2023**, *13*, 959. [CrossRef]
25. Baraj, E.; Ciahotný, K.; Hlinčík, T. The water gas shift reaction: Catalysts and reaction mechanism. *Fuel* **2021**, *288*, 119817. [CrossRef]
26. Busca, G. Acid Catalysts in Industrial Hydrocarbon Chemistry. *Chem. Rev.* **2007**, *107*, 5366–5410. [CrossRef]
27. Wang, X.; Rodriguez, J.A.; Hanson, J.C.; Gamarra, D.; Martínez-Arias, A.; Fernández-García, M. In Situ Studies of the Active Sites for the Water Gas Shift Reaction over $Cu-CeO_2$ Catalysts: Complex Interaction between Metallic Copper and Oxygen Vacancies of Ceria. *J. Phys. Chem. B* **2006**, *110*, 428–434. [CrossRef]
28. Ginsburg, J.M.; Piña, J.; El Solh, T.; De Lasa, H.I. Coke Formation over a Nickel Catalyst under Methane Dry Reforming Conditions: Thermodynamic and Kinetic Models. *J. Catal.* **2005**, *231*, 343–351. [CrossRef]
29. Zhang, X.; Zhang, Q.; Tsubaki, N.; Tan, Y.; Han, Y. Influence of zirconia phase on the performance of Ni/ZrO_2 for carbon dioxide reforming of methane. In *Advances in CO_2 Capture, Sequestration and Conversion*; ACS Publications: Washington, DC, USA, 2015; pp. 135–153.
30. Al-Fatesh, A.S.; Arafat, Y.; Kasim, S.O.; Ibrahim, A.A.; Abasaeed, A.E.; Fakeeha, A.H. In situ auto-gasification of coke deposits over a novel Ni-Ce/W-Zr catalyst by sequential generation of oxygen vacancies for remarkably stable syngas production via CO_2-reforming of methane. *Appl. Catal. B* **2021**, *280*, 119445. [CrossRef]
31. Chen, F.; Tao, Y.; Ling, H.; Zhou, C.; Liu, Z.; Huang, J.; Yu, A. Ni-Cu bimetallic catalysts on Yttria-stabilized zirconia for hydrogen production from ethanol steam reforming. *Fuel* **2020**, *28*, 118612. [CrossRef]
32. Jiang, W.; Loh, H.; Low, B.Q.L.; Zhu, H.; Low, J.; Heng, J.Z.X.; Tang, K.Y.; Li, Z.; Loh, X.J.; Ye, E.; et al. Role of oxygen vacancy in metal oxides for photocatalytic CO_2 reduction. *Appl. Catal. B* **2023**, *321*, 122079. [CrossRef]
33. Zhang, Y.; Zu, Y.; He, D.; Liang, J.; Zhu, L.; Mei, Y.; Luo, Y. The tailored role of "defect" sites on γ-alumina: A key to yield an efficient methane dry reforming catalyst with superior nickel utilization. *Appl. Catal. B* **2022**, *315*, 121539. [CrossRef]
34. Yu, S.; Hu, Y.; Cui, H.; Cheng, Z.; Zhou, Z. Ni-based catalysts supported on $MgAl_2O_4$ with different properties for combined steam and CO_2 reforming of methane. *Chem. Eng. Sci.* **2011**, *232*, 116379. [CrossRef]
35. Besenbacher, F.; Chorkendorff, I.; Clausen, B.S.; Hammer, B.; Molenbroek, A.M.; Nørskov, J.K.; Stensgaard, I. Design of a Surface Alloy Catalyst for Steam Reforming. *Science* **1998**, *279*, 1913–1915. [CrossRef]
36. Nørskov, J.K.; Abild-Pedersen, F.; Studt, F.; Bligaard, T. Density functional theory in surface chemistry and catalysis. *Proc. Natl. Acad. Sci. USA* **2011**, *108*, 937–943. [CrossRef]
37. Momin, N.; Manjanna, J.; Aruna, S.T.; Senthil Kumar, S.; Anjaneya, K.C. Effect of 20 mol % gadolinium doping on oxide ion conductivity of ceria as electrolyte for intermediate temperature solid oxide fuel cells. *Ceram. Int.* **2022**, *49*, 35867–35873. [CrossRef]
38. Fazlikeshteli, S.; Vendrell, X.; Llorca, J. Catalytic partial oxidation of methane over bimetallic Ru–Ni supported on CeO_2 for syngas production. *Int. J. Hydrogen Energy* **2023**, *51*, 1494–1507. [CrossRef]
39. Fakeeha, A.H. Strontium-Promoted Ni-Catalyst Supported over MgO for Partial Oxidation of Methane: Unveiling a Cost-Effective Catalyst System for Fast Mitigation of Methane. *Catalysts* **2025**, *15*, 814.
40. Fazlikeshteli, S.; Vendrell, X.; Llorca, J. Low-temperature partial oxidation of methane over Pd–Ni bimetallic catalysts supported on CeO_2. *Int. J. Hydrogen Energy* **2022**, *48*, 12024–12035. [CrossRef]
41. Al-Zahrani, S.A.; Bellahwel, O.; Ibrahim, A.A.; Alotibi, M.F.; Masood, N.; Rajeh, S.Y.; Otaibi, A.A.; Al-Enazy, H.D.A.; Al-Fatesh, A.S. Impact of Ga, Sr, and Ce on Ni/DSZ95 Catalyst for Methane Partial Oxidation in Hydrogen Production. *Catalysts.* **2024**, *14*, 851.
42. Alwadai, N.; Banabdwin, K.; Ali, D.A.; Osman, A.I.; Abahussain, A.A.; Elnour, A.Y.; Ibrahim, A.A.; Alarifi, N.; Ali, F.A.A.; Kumar, R.; et al. Methane partial oxidation with Ni-Mg-Al hydrotalcites: Impact of magnesium on catalyst performance. *Int. J. Green Energy* **2025**, *22*, 3855–3869. [CrossRef]

43. Oliveira, R.L.; Bitencourt, I.G.; Passos, F.B. Partial oxidation of methane to syngas on Rh/Al_2O_3 and $Rh/Ce\text{-}ZrO_2$ catalysts. *J. Braz. Chem. Soc.* **2013**, *24*, 68–75. [CrossRef]
44. Pantaleo, G.; La Parola, V.; Deganello, F.; Singha, R.K.; Bal, R.; Venezia, A.M. Ni/CeO_2 catalysts for methane partial oxidation: Synthesis driven structural and catalytic effects. *Appl. Catal. B Environ.* **2016**, *189*, 233–241. [CrossRef]

Disclaimer/Publisher's Note: The statements, opinions and data contained in all publications are solely those of the individual author(s) and contributor(s) and not of MDPI and/or the editor(s). MDPI and/or the editor(s) disclaim responsibility for any injury to people or property resulting from any ideas, methods, instructions or products referred to in the content.